

The contribution of the IGM and minihalos to the 21 cm signal of reionization

Bin Yue^{1,2,4}, Benedetta Ciardi², Evan Scannapieco³, Xuelei Chen¹

¹*National Astronomical Observatories, Chinese Academy of Sciences, 20A Datun Rd, Chaoyang District, Beijing 100012, China*

²*Max Planck Institute for Astrophysics, Karl Schwarzschild Str. 1; 85741 Garching; Germany*

³*School of Earth and Space Exploration, Arizona State University, P.O. Box 871404, Tempe, AZ, 85287-1404*

⁴*Graduate University of Chinese Academy of Sciences, 19A, Yuquan Road, Beijing 100049, China*

17 June 2009

ABSTRACT

We study the statistical properties of the cosmological 21 cm signal from both the intergalactic medium (IGM) and minihalos, using a reionization simulation that includes a self-consistent treatment of minihalo photoevaporation. We consider two models for minihalo formation and three typical thermal states of the IGM – heating purely by ionization, heating from both ionizing and Ly α photons, and a maximal “strong heating” model. We find that the signal from the IGM is almost always dominant over that from minihalos. In our calculation, the differential brightness temperature, δT_b , of minihalos is never larger than 2 mK. Although there are indeed some differences in the signals from the minihalos and from the IGM, even with the planned generation of radio telescopes it will be unfeasible to detect them. However, minihalos significantly affect the ionization state of the IGM and the corresponding 21 cm flux.

1 INTRODUCTION

The 21 cm signal from neutral hydrogen has the potential to provide a direct and independent probe of the cosmological gas distribution and its thermal and ionization states before and during reionization. Indirectly, such observations can be used to study the formation and evolution of early luminous sources, their feedback on the intergalactic medium (IGM), and their impact on the formation of subsequent generations of structures. As the 21 cm line is associated with the hyperfine transition in the ground state of neutral hydrogen, it depends on the distribution of atoms in these two energy levels, which is quantified by the spin temperature T_s . Since all the atoms are immersed in a sea of CMB radiation, in principle they can absorb or emit photons with the frequency corresponding to the energy splitting between the two hyperfine levels, $\nu_0 = 1.4204 \times 10^3$ MHz, possibly changing the shape of the CMB spectrum itself. If only CMB photons are present, absorption and emission equilibrate in a short time, and no line will be visible. However, there are other two mechanisms that can change the spin states of neutral hydrogen atoms – collisions and Ly α excitation (Wouthuysen-Field effect, Wouthuysen 1952; Field 1958), which render the 21 cm line visible in emission ($T_s > T_{\text{CMB}}$) or absorption ($T_s < T_{\text{CMB}}$) against the CMB background (e.g. Madau, Meiksin & Rees 1997).

The 21 cm signal from the high redshift universe has been studied in relation to minihalos (Iliev et al. 2002; Furlanetto & Oh 2006; Shapiro et al. 2006) and the IGM (e.g. Tozzi et al. 2000; Ciardi & Madau 2003; He et al. 2004; Furlanetto, Zaldarriaga & Hernquist 2004; Mellema et al. 2006; Santos et al. 2007). Prior to the

formation of radiation sources, the IGM is cold and neutral and the 21 cm line is expected to be observed in absorption against the CMB. Observations of the 21 cm signal at these very high redshifts would provide a wealth of information about the initial density fluctuations and the presence of a running spectral index or deviations from gaussianity (Loeb & Zaldarriaga 2004; Ali, Bharadwaj & Panday 2005; Pillepich, Porciani & Matarrese 2007; Lewis & Challinor 2007; Cooray, Li & Melchiorri 2008; Mao et al. 2008). Once the ionization sources turn on, they affect the 21 cm signal both by reducing the amount of neutral hydrogen and by increasing the temperature of the IGM through photoheating, Ly α photon scattering and, if the sources are hard enough, X-ray heating (Madau, Meiksin & Rees 1997; Oh 2001; Chen & Miralda-Escudé 2004; Chen & Miralda-Escudé 2008; Chuzhoy & Shapiro 2006; Furlanetto & Pritchard 2006; Chuzhoy & Shapiro 2007; Ciardi & Salvaterra 2007; Semelin, Combes & Baek 2007; Ripamonti, Mapelli & Zaroubi 2008). Eventually, such heating renders the IGM visible in emission.

A 21 cm signal is also expected from minihalos (MHs), collapsed structures with masses larger than the Jeans mass and smaller than the mass corresponding to a virial temperature of $\approx 10^4$ K. In such halos, the gas cannot cool efficiently unless a large fraction of molecular hydrogen is present. This, together with their fragility with respect to feedback effects (see e.g. Ciardi & Ferrara 2005) makes their contribution to star formation and photon production small at best. Nevertheless, MHs are expected to form copiously throughout cosmic history and their detection would be an observational breakthrough. It has been suggested that a possible way of detecting MHs is via the 21 cm line (Iliev et al.

2002; Furlanetto & Oh 2006; Shapiro et al. 2006). Because of their high density and temperature, MHs result in a signal that is expected to be different from that of the IGM. On one hand, collisions are frequent in such halos, coupling T_s to the gas temperature; on the other hand, the very dense gas can trap ionization fronts, protecting their central regions from being ionized. This makes MHs a possibly significant or even dominant source of 21 cm emission at some stage of cosmic history.

As MHs are expected to be found preferentially in high density regions, they are more likely to absorb UV radiation produced by nearby sources and get progressively photoevaporated (Shapiro et al. 1997; Shapiro & Raga 2000; Haiman et al. 2001; Barkana & Loeb 2002; Shapiro et al. 2004; Iliiev et al. 2005; Ahn & Shapiro 2007; Whalen et al. 2008). As a consequence, they can deplete the number of ionizing photons and delay IGM reionization. In addition to photoionization, MH formation and evolution is affected by a variety of feedback effects (see Ciardi & Ferrara 2005 for a complete review), whose relative importance has not been clearly established yet. Ciardi et al. (2006, C06 hereafter) performed the first simulations of reionization with a self-consistent treatment of MH photoevaporation, finding that, depending on the strength of the feedback effects, the presence of MHs could delay the end of reionization by as much as $\Delta z \approx 4$. In this paper, we use the results of these simulations to study the 21 cm signal from both the IGM and minihalos.

The layout of the paper is as follows. In Section 2 we give a short description of the C06 simulations and the method used to calculate the 21 cm signal from the IGM and the MHs. In Section 3 we present our results and discuss their uncertainties. In Section 4 we give our conclusions.

2 METHOD

In this Section we describe the method used to derive the 21 cm signal from the IGM and the MHs.

2.1 Simulations of reionization with minihalo photoevaporation

Here we give a short description of the simulation run in C06. Readers can find more details in the original paper and references therein.

The underlying N-body simulation was run in a cubic box of comoving length $L = 20h^{-1}\text{Mpc}$, which was extracted and resimulated from a much larger region (Yoshida, Sheth & Diaferio 2001). Galaxy formation was followed with a semi-analytic model (Kauffmann et al. 1999) and radiative transfer was calculated with the code CRASH (Ciardi et al. 2001; Maselli, Ferrara & Ciardi 2003; Maselli, Ciardi & Kanekar 2008), with the assumption that the gas follows the dark matter. This distribution was then mapped on a 128^3 grid, using the Triangular Shaped Cloud interpolation (Hockney & Eastwood 1981) to get the density in each cell. Throughout the simulation, the Efstathiou et al. (1992) transfer function was used and the cosmology was taken to be $(\Omega_m, \Omega_\Lambda, \Omega_b, h, \sigma_8, n) = (0.3, 0.7, 0.04, 0.7, 0.9, 1)$, where Ω_m , Ω_Λ , and Ω_b are the mean matter, vacuum, and baryonic densities in units of

the critical density, h is the Hubble constant in units of $100 \text{ kms}^{-1} \text{ Mpc}^{-1}$, σ_8 is the rms amplitude of matter fluctuations on the $8 \text{ Mpc } h^{-1}$ scale, and n is the slope of the primordial power spectrum.

Unlike the original simulations by Ciardi, Stoehr & White (2003) and Ciardi, Ferrara & White (2003), in C06 sub-grid physics was included to take into account the effects of MHs on reionization. Generally speaking, the box size of a reionization simulation should be large enough to be representative of the whole universe. This requirement makes it impractical to resolve individual minihalos (whose mass may be as small as $10^5 M_\odot$). For this reason, C06 used a “sub-grid correction” to include their effects on reionization, which are mainly due to two issues:

- 1) Gas accretion onto MHs, which reduces the density of the IGM;
- 2) MHs absorption of photons that would otherwise ionize the IGM. Because of their high gas density and recombination rate, MHs can consume many more photons than the IGM, relative to their overall mass fraction.

To take into account the above effects, at each step of the simulation in C06, the following “sub-grid correction” was applied:

- In each cell, the total mass of MHs was calculated using the Extended Press-Schechter (EPS) theory (Lacey & Cole 1993; Mo & White 1996; Sheth & Tormen 2002)¹, and the IGM density was corrected accordingly.

- The number of ionizing photons absorbed by MHs in each cell was taken to be:

$$N_{\gamma, \text{MH}} = N_\gamma (1 - e^{-\tau_{\text{MH}}}), \quad (1)$$

where τ_{MH} is the optical depth of MHs, which is proportional to the mass fraction of MHs $f_{\text{coll, MH}}$, and N_γ is the number of photons injected into this cell.

- At each step, the fraction of minihalos photoevaporated was computed as:

$$\mathcal{F}_{\text{MH, eva}} = \frac{N_{\gamma, \text{MH}}}{n_{\text{H}} \Delta l^3 \xi}, \quad (2)$$

where n_{H} is the hydrogen number density, Δl is the size of one cell, while ξ is the average number of photons consumed by minihalos per total atom (the expressions can be found in the original paper).

As mentioned in the introduction, the detailed effect of feedback on MH formation and evolution is still unknown. For this reason C06 have considered two extreme models in the simulations. The first is the extreme suppression (ES) model, in which once a cell has been crossed by an ionizing photon, no new halos are allowed to form within it unless it recombines to become completely neutral. The second is the reformation model (RE), in which MHs continue to form undisturbed by feedback effects. The real situation is expected to lie between these two extreme cases.

¹ A slightly different prescription is used in cells hosting sources, but their impact is minor.

2.2 21 cm signal from the IGM

The differential brightness temperature δT_b of the IGM is calculated following Ciardi & Madau (2003) (see also Furlanetto & Loeb 2002; Mellema et al. 2006; Shapiro et al. 2006):

$$\delta T_b = 0.016T \left(1 - \frac{T_{\text{CMB}}}{T_s} \right) \text{K}, \quad (3)$$

where

$$T = \frac{1}{h} (1+\delta)(1-f_{\text{coll,MH}})(1-x) \left(\frac{\Omega_b h^2}{0.02} \right) \left[\left(\frac{1+z}{10} \right) \left(\frac{0.3}{\Omega_m} \right) \right]^{1/2}, \quad (4)$$

with x ionization fraction. This formula is accurate only in the optically thin limit, which is appropriate for the IGM. T_s is the spin temperature, which determines the distribution of neutral hydrogen atoms in the two hyperfine levels. The value of T_s is a weighted mean between the CMB temperature, T_{CMB} , and the gas kinetic temperature, T_k , and depends on the effect of collisions and Ly α pumping. In this work we use

$$T_s = \frac{T_{\text{CMB}} + (y_{\alpha,\text{eff}} + y_c)T_k}{1 + y_{\alpha,\text{eff}} + y_c}, \quad (5)$$

where y_c is the collisional coupling efficiency (including H-H, H-e⁻ and H-p collisions; see Nusser 2005; Kuhlen, Madau & Montgomery 2006), and $y_{\alpha,\text{eff}}$ is an effective Ly α coupling efficiency term that can be written as (Chuzhoy & Shapiro 2006):

$$y_{\alpha,\text{eff}} = y_\alpha \exp \left[-0.3(1+z)^{1/2} T_k^{-2/3} \right] \left(1 + \frac{0.4}{T_k} \right)^{-1}, \quad (6)$$

where y_α is the standard Ly α coupling efficiency (Madau, Meiksin & Rees 1997). The IGM temperature in the absence of heating mechanisms has been calculated using RECFAST (Seager, Sasselov & Scott 1999, 2000).

Typically, the IGM can be found in three thermal states, which define the value of the differential brightness temperature, as listed below:

1) *No heating.* In this state, which occurs before and during the early stages of structure evolution, the IGM cools adiabatically. As long as the density of neutral hydrogen is high enough, collisions between different atoms couple T_s to T_k , which is usually lower than T_{CMB} at that stage, so that the 21 cm signal is in absorption. However, following the expansion of the universe, the density decreases as $\propto (1+z)^3$, so that collisional coupling becomes ineffective below $z \approx 20$. In this case, the spin temperature is only slightly smaller than T_{CMB} .

2) *Ly α and UV photon heating.* Once the first sources of radiation turn on, their UV photons start to ionize and heat the surrounding gas. While their impact is limited to the regions in the immediate vicinity of the sources, the Ly α photons (both continuum and injected; see Chen & Miralda-Escudé 2004; Chen & Miralda-Escudé 2008) can travel much further from their production sites because of the longer mean free path compared to UV photons, and quickly build up a background that can influence the IGM as a whole. The Ly α photons have a double effect on the spin temperature. First, even a small Ly α intensity ($\approx 10^{-20} \text{erg cm}^{-2} \text{s}^{-1} \text{Hz}^{-1} \text{sr}^{-1}$) can make y_α in eq. (6) much larger than 1 and bring T_s very close to T_k , so that the spin

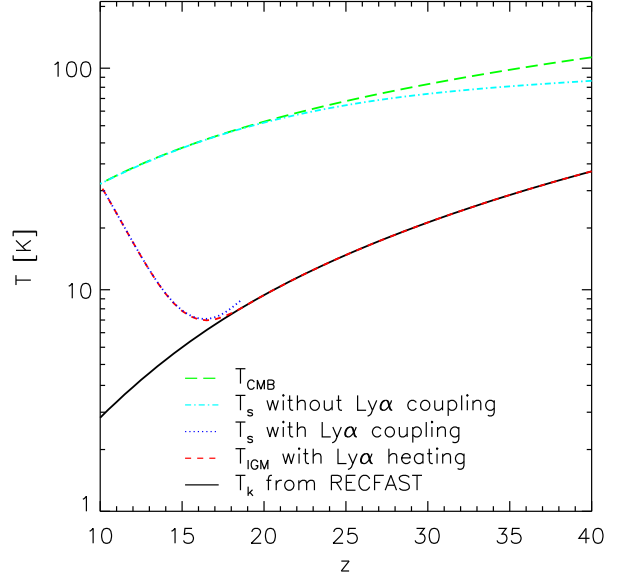


Figure 1. Evolution of CMB temperature (long-dashed line), IGM temperature in the absence of heating mechanisms (solid), with Ly α heating (short-dashed), spin temperature without (dashed-dotted line) and with (dotted) Ly α coupling. Ly α photons are included only from the start of the simulation, i.e. from $z = 18.5$.

temperature traces the state of the IGM. This effect is typically referred to as Ly α coupling or the Wouthuysen-Field effect.

Secondly, Ly α photons can heat or cool the IGM slightly by resonance scattering, as has been studied by several authors (Madau, Meiksin & Rees 1997; Chen & Miralda-Escudé 2004; Rybicki 2006; Furlanetto & Pritchard 2006). Recent works (Chen & Miralda-Escudé 2004; Rybicki 2006; Furlanetto & Pritchard 2006; Meiksin 2006) find lower values than originally estimated (Madau, Meiksin & Rees 1997). Nevertheless, it may still have some impact on the thermal evolution of the IGM (Ciardi & Salvaterra 2007). In this paper we calculate this effect with the Ly α background derived in Ciardi & Madau (2003), which is self-consistent with the simulation of C06. Figure 1 shows the temperature evolution of a homogeneous cosmic density field. The dashed-dotted line is the spin temperature without any heating mechanisms, while the dotted line is the spin temperature used in our Ly α heating case. Both estimates exclude the photoionization heating. With the adopted Ly α flux background, the temperature of the IGM is never higher than T_{CMB} before the end of reionization. Thus, as Ly α heating is not extremely efficient, we expect a 21 cm signal in absorption.

3) *Strong heating.* Finally, when the Ly α background becomes strong enough or additional sources of heating are present, we expect the temperature T_k to become much larger than T_{CMB} . Such high temperatures could be reached in the presence of X-rays, that can heat the IGM above 1000 K (Chen & Miralda-Escudé 2004; Chen & Miralda-Escudé 2008; Furlanetto & Oh 2006; Furlanetto, Oh & Briggs 2006). Although there are still

some uncertainties on the extent of the X-ray background, it seems plausible to have $T_s \gg T_{\text{CMB}}$ at later times during cosmic evolution. In this situation, the 21 cm signal is always in emission (Zaldarriaga, Furlanetto & Hernquist 2004; Santos, Cooray & Knox 2005).

In addition to X-rays, Ly α and UV photons, shocks due to structure formation can also heat the IGM (Furlanetto & Loeb 2004; Miniati et al. 2004; Shapiro et al. 2006). Shock heating may be significant if the gas is still cold at high redshift (Furlanetto, Oh & Briggs 2006). However, Shapiro et al. (2006) showed that even taking into account shock heating, the 21 cm signal from MHs is still larger than that from the IGM at $z < 20$. In fact, shock heating usually is efficient around large halos or in high density regions. The same regions however are also likely to be ionized by nearby sources. This may suppress the effect of heating by shocks. Also, C06 did not consider shock heating because they assumed the gas to trace the dark matter distribution. So this contribution is not considered further in the present work.

The details about the transition between these three configurations are still not clear, mainly because of our persistent ignorance on the details associated with the heating mechanism. Here, we estimate the 21 cm signal in three heating case: pure UV heating, Ly α and UV heating and strong heating. The UV heating is treated as did in the simulation by C06.

2.3 21 cm signal from MHs

In principle, the differential brightness temperature of MHs can be derived by replacing \mathcal{T} in eq. (4) with:

$$\mathcal{T}_{\text{MH}} = \frac{1}{h}(1+\delta)f_{\text{coll,MH}}(1-x) \left(\frac{\Omega_b h^2}{0.02} \right) \left[\left(\frac{1+z}{10} \right) \left(\frac{0.3}{\Omega_m} \right) \right]^{1/2}, \quad (7)$$

which is proportional to the mass fraction of MHs.

However, this formula is valid only in the optically-thin case, while the optical depth of an individual minihalo is usually large. In fact, for a halo with mass $10^5 M_\odot$, the typical value of the optical depth along a line-of-sight across the center of the halo is ≈ 0.5 (Iliev et al. 2002), and it drops as the mass increases because of the high T_s and the low absorption coefficient of high mass halos (see Iliev et al. 2002). Iliev et al. (2002) give the more appropriate result of 21 cm flux and δT_b for an optically-thick case, assuming that the halo is a Truncated Isothermal Sphere (TIS; Shapiro, Iliev & Raga 1999; Iliev & Shapiro 2001). In this paper we make use of their results.

Because of their high density and temperature (compared with T_{CMB}), individual MHs are expected to always produce a 21 cm signal in emission (Shapiro et al. 2006), with a large δT_b (in Fig. 1 of Iliev et al. 2002, the typical value is several hundred mK at frequency $\nu_0 = 1.4204 \times 10^3$ MHz, and even larger after integration along the line profile). However, it is extremely difficult to resolve individual halos, because their angular size is usually less than $1''$. For this reason it is customary to estimate, rather than the signal from individual halos, the beam-averaged effective differential brightness temperature as (eq. (6) in Iliev et al. 2002):

$$\delta \bar{T}_b = \frac{c(1+z)^4}{\nu_0 H(z)} \int_{M_{\text{min}}}^{M_{\text{max}}} \Delta \nu_{\text{eff}} \delta T_{b,\nu_0} A \frac{dn}{dM} dM, \quad (8)$$

where dn/dM is the mass function of minihalos and $H(z)$ is the Hubble parameter. Here we take the Jeans mass as the lower mass limit, which is

$$M_{\text{min}} = 5.7 \times 10^3 \left[\frac{\Omega_m h^2}{0.15} \right]^{-\frac{1}{2}} \left[\frac{\Omega_b b^2}{0.02} \right]^{-\frac{3}{8}} \left(\frac{1+z}{10} \right)^{\frac{3}{2}}, \quad (9)$$

as in Shapiro et al. (2006). The upper mass limit is $M_{\text{max}} = 2.8 \times 10^9 (1+z)^{-3/2} M_\odot$, which corresponds to $T_{\text{vir}} = 10^4$ K in our cosmology. $A = \pi r_{\text{TIS}}^2$ is the geometric cross section of a halo, where r_{TIS} is the truncated radius in the TIS model (Iliev & Shapiro 2001); $\Delta \nu_{\text{eff}}(z) = [(2\pi\mu)^{1/2} \nu_0 \sigma_v / c] / (1+z)$ is the redshifted effective line width and $\delta T_{b,\nu_0}$ is the differential brightness temperature of a single halo at the frequency ν_0 (the detailed expressions can be found in Iliev et al. 2002).

While dn/dM can be derived from a Press-Schechter approach, in this case, we need also to account for photoevaporation of the MHs. While the simulations described in Section 2 provide the total MHs mass fraction in each cell at any given time, we have no information on the distribution of mass amongst the MHs. We thus proceed as follows. In Iliev et al. (2005) it is shown that the mass evolution of an individual halo exposed to a flux $F_0 = F / \{10^{56} \text{s}^{-1} / [4\pi(1\text{Mpc})^2]\}$, with an initial mass M_0 at redshift z_0 , is a function $M = M(M_0, z_0, z, F_0)$. The function can be inverted to derive $M_0 = M_0(M, z_0, z, F_0)$, i.e. from the mass of a halo we can get the mass of its progenitor. Then, at any redshift and in any given cell, the minihalo mass function, including photoevaporation, can be written as:

$$\begin{aligned} \frac{dn}{dM}(M, z) &= \int_{z_{\text{cr}}}^z \frac{d^2 n}{dM_0' dz'}(M_0', z') \times \\ &\quad \frac{dM_0'}{dM}(M_0', M, z', z, F_0) dz' \\ &+ \frac{dn}{dM_0}(M_0, z_{\text{cr}}) \frac{dM_0}{dM}(M_0, M, z_{\text{cr}}, z, F_0). \end{aligned} \quad (10)$$

Here, z_{cr} is the redshift at which a photon packet crosses the cell for the first time and $M_0' = M_0(M, z', z, F_0)$. The first term of the equation takes into account the evolution of the mass function due to all the halos forming between z_{cr} and z , while the second term describes the evolution in the mass function of halos already in place at z_{cr} . Both $d^2 n / dM_0' dz'(M_0', z')$ and $dn/dM_0(M_0, z)$ are calculated with the EPS theory, following C06. The equation above is valid in the reformation case, while in the extreme suppression model, once a cell has been crossed by ionizing photons, no new halo can form. In this case, the first term of the equation should be set to zero.

Throughout the paper, we use the mass photoevaporation law of Iliev et al. (2005), which is:

$$M(t) = M_0 \left(1 - \frac{t}{C t_{\text{ev}}} \right)^B. \quad (11)$$

In this equation, C and B are parameters determined by the spectrum of the sources. In our case $C = 1.07$ and $B = 2.5$ (Iliev et al. 2005). The evaporation time $t_{\text{ev}} = t_{\text{ev}}(F_0, M_0, z_{\text{cr}})$ is a function of F_0 , M_0 , z_{cr} and of the source spectrum. Figure 2 shows the mass evolution of individual halos with different initial masses, M_0 , at $z_0 = 17.6$, exposed to various constant fluxes of $F_0 = 0.01, 1$, and 1000 .

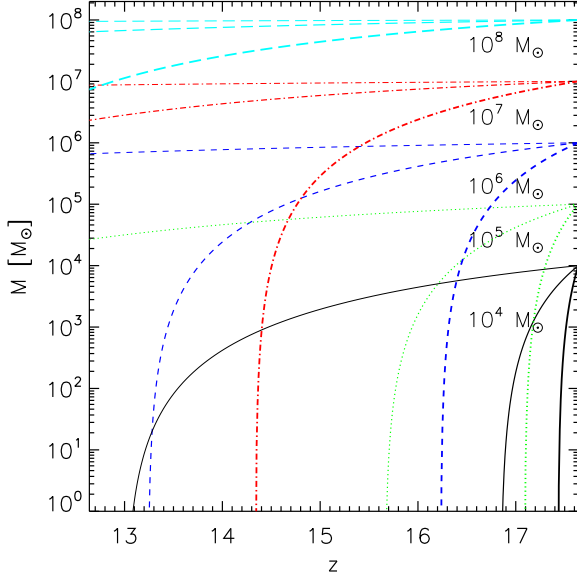


Figure 2. Redshift evolution of the remaining mass of halos with different initial mass, under the effect of a photoevaporating flux with $F_0 = 0.01, 1, 1000$ (from top to bottom in each line group). The initial (at $z_0 = 17.6$) mass of the halos, M_0 , is as labelled.

While low-mass halos disappear on very short time scales (≈ 14 Myrs if $F_0 = 1$ and $M_0 = 10^4 M_\odot$), larger mass halos retain most of their mass. For example, with $F_0 = 1$, a halo with $M_0 = 10^8 M_\odot$ will have a mass $M = 6 \times 10^7 M_\odot$ after 126 Myrs, i.e. has undergone a mass loss of only 40%.

In principle, if the flux evolution in each cell is known, it is possible to re-construct the mass evaporation process for halos in each mass bin according to eq. (11). In C06, the flux is determined by sources in the simulation box (Ciardi et al. 2001, 2006). However, as it is computationally unfeasible to record the value of F_0 in each cell at each timestep of the simulation, we only recorded the total evaporated mass fraction of minihalos in each cell. We then adopt an effective ionization flux which gives identical evaporated mass fraction as F_0 , to calculate the mass evolution of halos with different mass. Two methods are used to get the effective flux and implement eq. (11). In the first, in each cell and at each time step of the simulation, z^i , we use an effective ionization flux, $F_{0,eff}^i$, which is assumed to be constant between z_{cr} and z^i . As we know the total mass of MHs in the cell, $M_{tot}^i = \sum_j M_j(t^i)$, we use the following equation:

$$M_{tot}^i = \sum_j M_{0,j} \left(1 - \frac{t^i}{Ct_{ev}(F_{0,eff}^i, M_{0,j}, z_{cr})} \right)^B, \quad (12)$$

where the sum is performed over all the MHs in the cell. The above equation is solved to derive the only unknown quantity $F_{0,eff}^i$, which is then used in eq. (10) to calculate the re-distributed MH mass function and $\delta\bar{T}_b$. At the following time step, the same process is repeated to derive a new effective flux.

In the second method, we also choose an effective flux for each cell. Differently from the first method, here the effective flux evolves step by step, rather than being constant

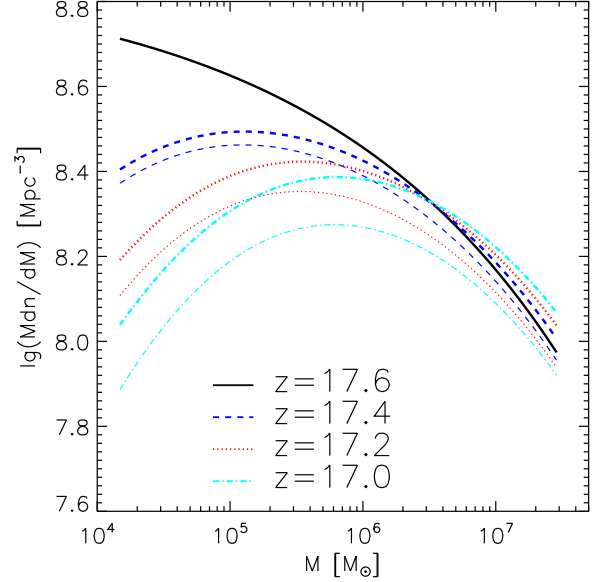


Figure 3. The evolution of the mass function under photoevaporation for the extreme suppression model (thin lines) and the reformation model (thick lines). From top to bottom, the lines correspond to redshift 17.6 (when the evaporation begins), 17.4, 17.2 and 17.0 respectively. Here we assume a constant flux $F_0 = 1$.

from z_{cr} to z^i . At each time step, z^i , we calculate:

$$M_{tot}^{i-1} - M_{tot}^i = \sum_j \Delta M_j^i, \quad (13)$$

where:

$$\Delta M_j^i = M_{0,j} \left[\left(1 - \frac{t^{i-1}}{Ct_{ev}(F_{0,eff}^{i-1}, M_{0,j}, z_{cr})} \right)^B - \left(1 - \frac{t^i}{Ct_{ev}(F_{0,eff}^i, M_{0,j}, z_{cr})} \right)^B \right], \quad (14)$$

is the mass of minihalo j evaporated between two steps. From the above equations we derive the only unknown quantity, $F_{0,eff}^i$ and then we use it in eq. (10) to calculate the re-distributed MH mass function and $\delta\bar{T}_b$. Also, the same process is repeated to derive a new effective flux at the following time step. We have used both methods and found that the results are consistent with each other, as in the vast majority of cells at any time the difference in the $\delta\bar{T}_b$ obtained with the two methods is less than 5%. Thus, in the following we will always use the first one.

Figure 3 instead shows the mass function at different redshifts with the assumption of a constant ionization flux $F_0 = 1$, as calculated in eq. (10). The thin lines refer to the extreme suppression model, while the thick lines are the reformation model. As expected, the mass function in the reformation model is always larger than that in the extreme suppression model. In the former, at high mass end, the formation rate of halos is higher than the evaporation rate, so the mass function increases with time.

Using the above mass functions, we can now calculate the expected differential brightness temperature. Figure 4 shows the mean (volume-averaged) $\delta\bar{T}_b$ evolution for the two MH formation models, which has been calculated both with

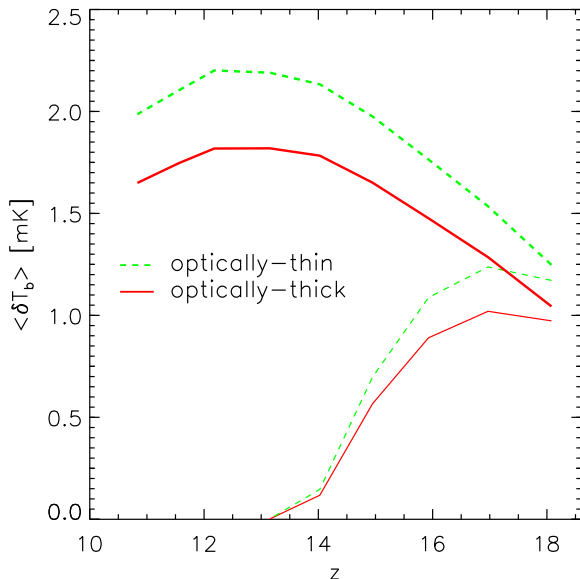


Figure 4. Evolution of the volume-averaged δT_b of minihalos from the simulations described in Ciardi et al. (2006). The solid (dashed) lines refer to an optically thick (thin) case. The thin (thick) lines refer to the extreme suppression (reformation) model for minihalo evolution.

the optically-thin formula given in eq. (3) with the assumption that $T_s \gg T_{\text{CMB}}$ (dashed lines) and for the optically-thick case in eq. (8) (solid lines), with $\delta T_{b,\nu_0}$ taken from Figure 1 of Iliev et al. (2002). Although the δT_b for an individual halo is very high compared with the optically-thin case, the beam-averaged $\delta \bar{T}_b$ is very small (with a typical value of $\approx 1\text{--}2$ mK). This is because the halos usually have a small geometric cross section A , and thus the associated flux is not very significant. Figure 4 also shows that the optically thin assumption with $T_s \gg T_{\text{CMB}}$ is a good approximation to calculate the mean 21 cm signal from minihalos. δT_b in the extreme suppression model drops dramatically following the evaporation of the minihalos. In the reformation model instead, it increases continuously until late times. Thus, the presence or absence of MH reformation can result in totally different pictures of the evolution of the 21 cm signal from MHs.

3 RESULTS AND ANALYSIS

In this Section we present our results in terms of mean differential brightness temperature (as described in Secs. 2.2 and 2.3) and fluctuations of brightness temperature, and we discuss their uncertainties. As a visual example, in Figure 5 we show maps of the δT_b in the pure UV heating case and reformation model. From top to bottom, the three rows correspond to the IGM, MHs, and the total. The map shows that at the early and late stages of reionization, MHs contribute more to the total signal compared with the IGM, while at intermediate redshifts the contribution from partially ionized IGM increases.

3.1 Mean differential brightness temperature

The contribution from MHs to the mean differential brightness temperature is calculated as described in the previous Section and is shown as dashed-dotted lines in Figure 6. The two formation models for MHs (ES and RE) represent two extreme effects of the IGM heating on the 21 cm signal from MHs. In each model, the signal of MHs does not vary as a function of IGM heating, so these lines are the same as the solid lines in Figure 4. δT_b from MHs is roughly proportional to the total mass of MHs, while it is not sensitive to the shape of their mass function. On the other hand, the IGM contribution strongly depends on its thermal state, and we present results for three different cases.

First, we discuss the case in which only heating from ionizing radiation is present. Over the redshift range covered by the simulations, the collisional coupling in the mean-density IGM considered here is very weak. Thus, in the absence of other decoupling mechanisms, the spin temperature of neutral hydrogen is very close to T_{CMB} and the 21 cm line is only slightly visible in absorption (dashed lines in Fig. 6). However, as the first sources of radiation turn on and reionization begins, the energy of the ionizing photons heats the IGM in the vicinity of the sources to a significant high temperature (in this work we follow C06 and use the reference value 10^4K , which is a reasonable approximation in regions ionized by stellar type sources; see Ciardi et al. 2001; Pritchard & Furlanetto 2007). Thus the IGM in such regions may emit 21 cm radiation until it has been fully ionized, so that the mean δT_b changes from a negative to a positive value. However, as reionization proceeds, the amount of neutral hydrogen decreases and the mean δT_b drops to zero again.

In the extreme suppression case, we find that even in the presence of only collisional decoupling and UV heating, the 21 cm signal from minihalos dominates the total signal only in the very early stages of reionization. This is because reionization suppresses the formation of new minihalos and photoevaporates existing ones, reducing their contribution with time. On the other hand, reionization increases the temperature of the partially-ionized IGM and the density of free electrons. In high temperature, partially ionized regions, H-e^- and H-p collisions are more effective than H-H collisions in coupling T_s to T_k . As a consequence, the fraction of flux from partially ionized gas is higher than its volume filling factor, and the signal from the IGM increases with time until a volume averaged ionized fraction of $x_{\text{HII}} \approx 0.5$ has been reached, at $z \approx 15$, which corresponds to a peak of the emission.

On the other hand, in the reformation model, the flux from the IGM is reduced by the significant value of $f_{\text{coll,MH}}$ and pushed towards lower redshift by the delay in the reionization process. In this case, the period during which the flux from minihalos is larger than that from the IGM is extended to $\Delta z \approx 4$, and reaches a peak at $z \approx 12$.

It should be stressed that the signal from the IGM dominates over that from the MHs because of the collisions between atoms and free electrons and protons (we discuss the uncertainties of this in Sec. 3.3). In fact, if we ignore this contribution, the peak of δT_b from the IGM is only ≈ 2 mK and the signal from MHs dominates down to $z \approx 15.5$ in

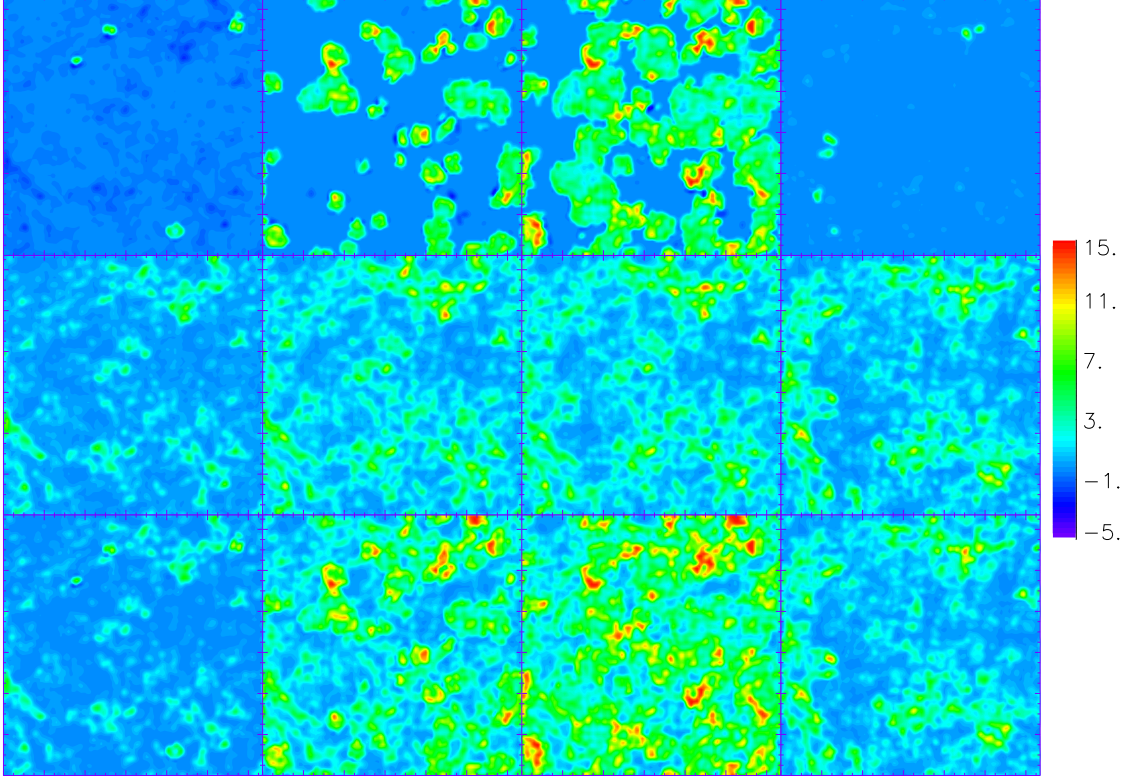


Figure 5. A map of δT_b in units of mK in the pure UV heating case and reformation case (see text for details). From top to bottom, the three rows correspond to the IGM, MHs, and the total. In each row, from left to right, the panels show slices at redshift 18.5, 14.6, 12.8, 10.6 respectively. The comoving thickness of the slice corresponds to the dimension of one cell in the simulation, i.e. ≈ 223 kpc.

the extreme suppression model, and at almost all redshifts in the reformation model.

Next, we consider a case that includes the effects from a $\text{Ly}\alpha$ background, leading to the mean δT_b evolution shown in Figure 7. Here we see that the $\text{Ly}\alpha$ background produced by the sources in the simulation is strong enough to couple T_s to T_k and to heat the IGM above the adiabatic temperature, but the mean temperature is still below T_{CMB} . This induces a strong mean signal in absorption, and a minimal emission is visible only at a late evolutionary stage in the reformation model. This is because reionization proceeds to lower redshift, when more sources form and produce a larger value of the $\text{Ly}\alpha$ background. Yet even in this case the bulk of the emission is due to the partially-ionized regions.

The reason for the very different behavior compared to the no $\text{Ly}\alpha$ background case is the following. Without $\text{Ly}\alpha$ photons the contribution to δT_b consists of a small negative signal from the neutral, cold IGM (because $T_s \approx T_{\text{CMB}}$), and a positive signal from the the partially ionized, hot IGM. In the presence of $\text{Ly}\alpha$ photons instead, the dominant contribution comes from a strong negative signal from the the neutral, warm IGM (because $T_s \ll T_{\text{CMB}}$) which exceeds the smaller positive signal from the partially ionized, hot IGM. In this case we find that the IGM signal always dominates the total signal consistent with Furlanetto & Oh (2006).

Finally, we consider a situation in which $T_s \gg T_{\text{CMB}}$, resulting in the evolution of the mean δT_b shown in Figure 8. As expected, in this case δT_b is always positive and it decreases as reionization proceeds and the available neutral hydrogen is depleted. Unlike the cases analyzed before, the signal corresponding to the extreme suppression model is always lower than that of the reformation model. This is due to the fact that, in this case, δT_b is independent of T_s and depends only on the amount of neutral hydrogen present at each redshift, which is higher in the reformation model. Moreover, the signal from the IGM always dominates over that from the MHs. This is because in both cases the condition $T_s \gg T_{\text{CMB}}$ is satisfied, meaning that $\delta T_{b,\text{IGM}} \propto f_{\text{IGM,HI}}$ and $\delta T_{b,\text{MH}} \propto f_{\text{MH,HI}}$, with a similar constant of proportionality. Thus $f_{\text{IGM,HI}} \gg f_{\text{MH,HI}}$ implies $\delta T_{b,\text{IGM}} \gg \delta T_{b,\text{MH}}$.

3.2 rms fluctuations and pixel distribution

We now calculate the rms fluctuations in the brightness temperature distribution, $\langle (\delta T_b - \langle \delta T_b \rangle)^2 \rangle^{1/2}$, as a function of the beamsize, $\Delta\theta$, and redshift. We choose a slice corresponding to a bandwidth $\Delta\nu = 0.1$ MHz, located at the center of the simulation box. A larger bandwidth (e.g. 1 MHz) would produce lower fluctuations because in that case inhomogeneities

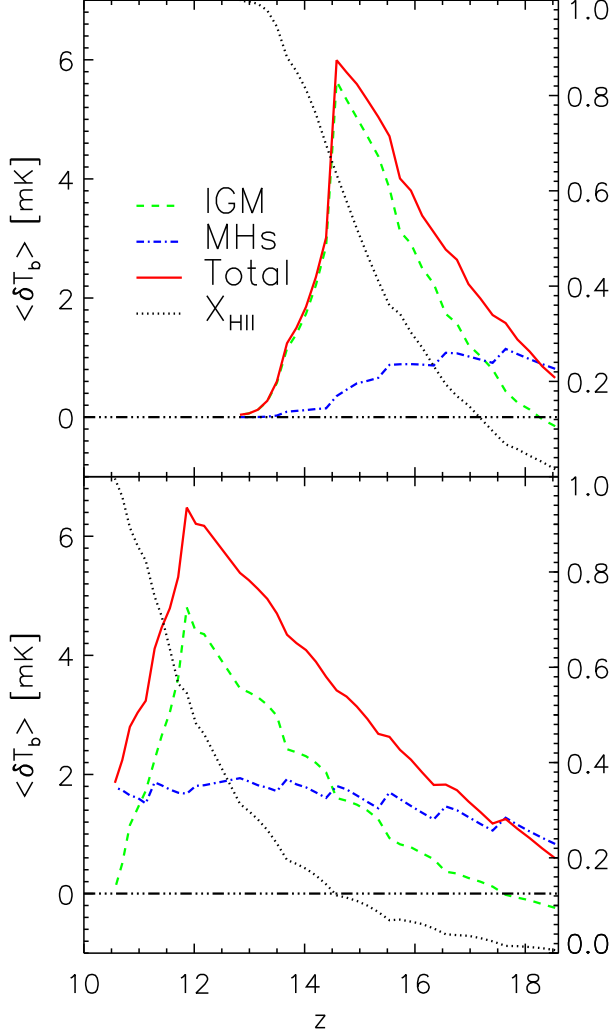


Figure 6. Mean δT_b evolution in the absence of heating sources, with the exception of the UV ionizing radiation. The solid, dashed, dashed-dotted and dotted lines refer respectively to the contribution of IGM+MHs, only IGM, only MHs and the volume averaged ionization fraction. The top panel refers to the extreme suppression model, while the bottom panel refers to reformation model. To guide the eye, we also plot a horizontal line corresponding to $\delta T_b = 0$.

in the gas density and in the hydrogen ionized fractions would be more poorly resolved (see e.g. Ciardi & Madau 2003).

The results are shown in Figure 9 and 10, for the three IGM thermal states and two MH formation models described in the previous Sections. Figure 9 gives the rms as a function of beamsize at several different redshifts for both the reformation (upper panels) and the extreme suppression (bottom panels) model. Figure 10, instead, gives the evolution of rms for different beamsize in the same two models. In all cases, the signal increases as the angular scale decreases because the mass variance is larger on small scales. Another common feature is that, although the continuous formation

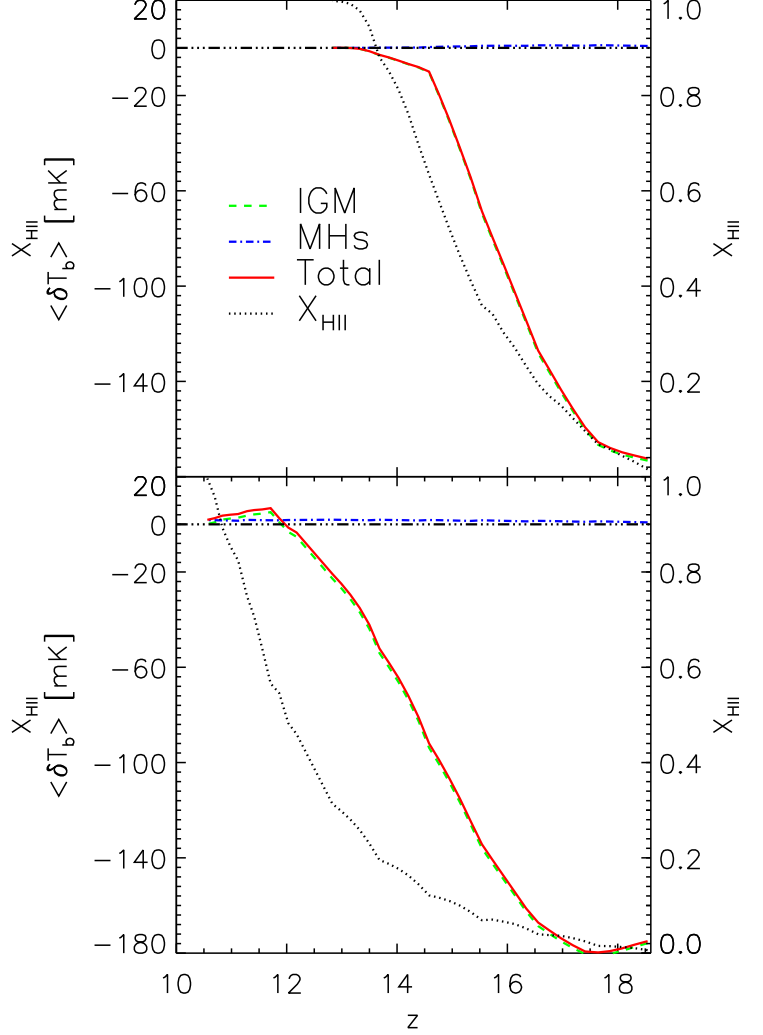


Figure 7. As Fig. 6 but including heating by $\text{Ly}\alpha$ photons.

of minihalos increases the signal compared to the extreme suppression case, it does not increase the inhomogeneity of the gas, so the rms in the reformation model is similar to the rms of the extreme suppression model until the latter drops because of reionization.

In the pure UV heating case, the signal from the IGM reaches a maximum at $z \approx 14$ (extreme suppression model) and at $z \approx 12$ (reformation model), corresponding to the epoch when several neutral regions are still present, but the volume is roughly half ionized. Then it starts decreasing and drops dramatically when the IGM gets close to complete reionization. The signal from the MHs shows a similar behavior, but in the reformation model the drop associated with photoevaporation is not evident because they are allowed to continuously reform. The general trend in the relative importance of the IGM and MHs contribution follows what already seen in the mean brightness temperature, i.e. the MHs contribution dominates in both models in the earliest stages of the evolution and when reionization is almost complete in the reformation model. Otherwise the

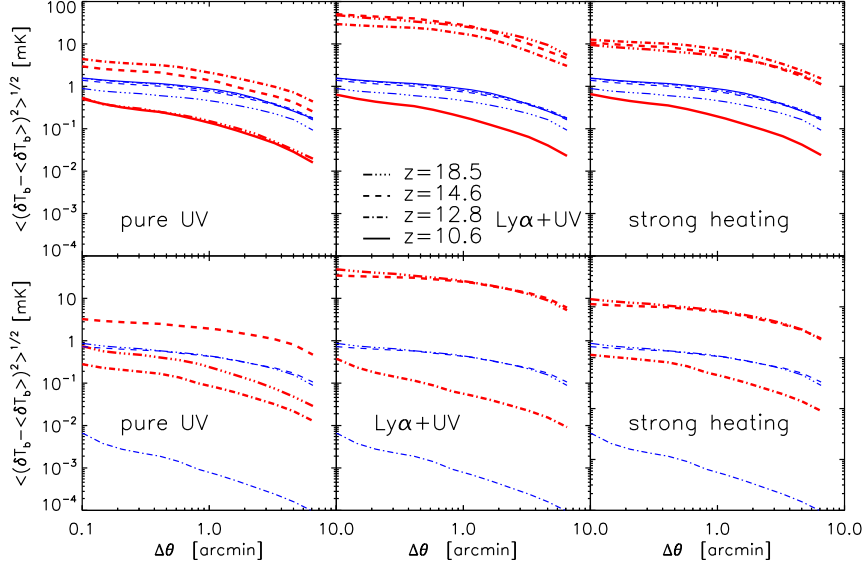


Figure 9. Expected rms brightness temperature fluctuations as a function of beamsize at different redshift. Upper and lower panels refer to the reformation and extreme suppression models, respectively. The three thermal states of the IGM are labeled in each panel. Thick (thin) lines refer to the IGM (MHs) contribution, at the redshifts 18.6, 14.6, 12.8, and 10.6.

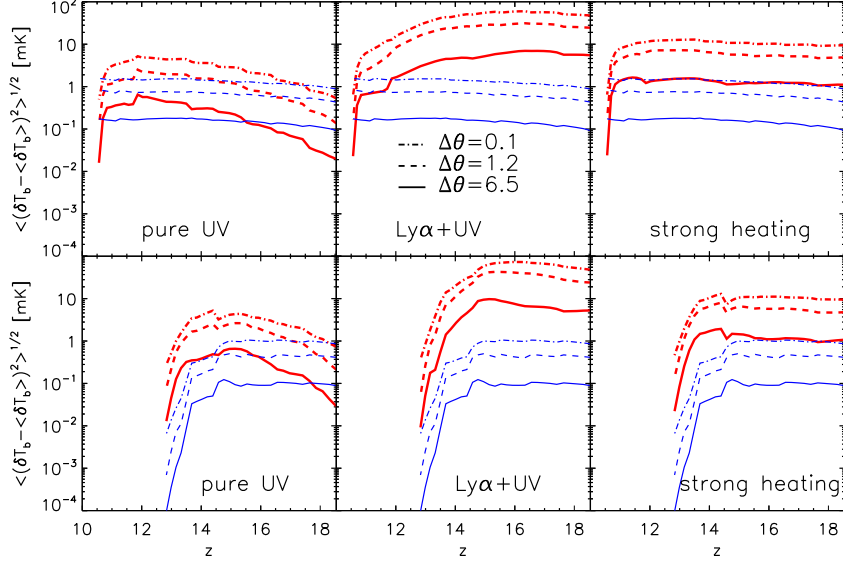


Figure 10. Expected rms brightness temperature fluctuations as a function of redshift with different beamsize. The meaning of each panel is the same as in Fig. 9.

IGM contribution is dominant. In addition, the smaller the beamsize, the earlier the fluctuations that from IGM exceed those from the MHs². Thus, increasing the resolution of the beam might not help in detecting the signal from MHs (because observations at higher redshift and lower frequencies are more difficult), unless one chooses a region particularly rich in MHs.

² Here we only consider $\Delta\theta = 0.1'$ because this corresponds to the size of one cell in the simulation.

Also in the $T_s \gg T_{\text{CMB}}$ case and in the Ly α case, the behavior of the rms is similar to that of the mean brightness temperature, with the MH signal dominating only in the reformation model during the latest stages of reionization.

We then calculate the pixel distribution of the brightness temperature, $\delta T_b df / d\delta T_b$, as a function of δT_b for the IGM in the three cases and minihalos. Here $df = N_{\delta T_b} / N_{\text{tot}}$, where N_{tot} is the total number of cells in the simulation box and $N_{\delta T_b}$ is the number of cells that lie in the bin $d\delta T_b$. In Figure 11 and 12 the panels correspond, from left to right

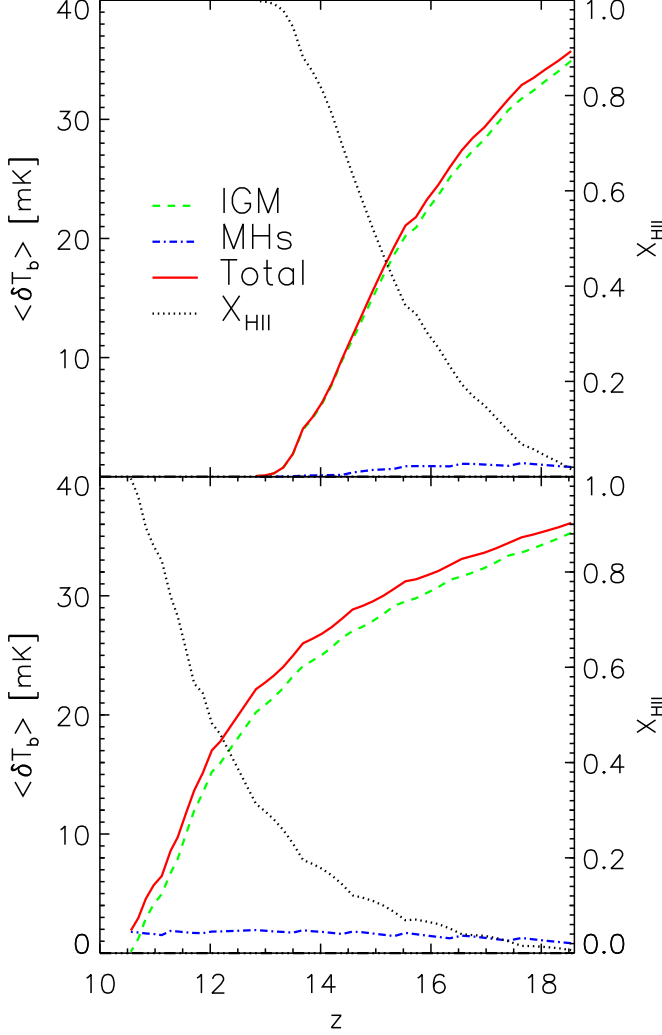


Figure 8. As Fig. 6 but in the $T_s \gg T_{\text{CMB}}$ case.

and from top to bottom, to pure UV heating case, Ly α heating case, $T_s \gg T_{\text{CMB}}$ case and minihalos, respectively.

The amplitude of the pixel distribution indicates the relative contributions from different δT_b bins to the total signal. The double peaks associated with the two-phase structure of the IGM (totally neutral and partially ionized regions) are very prominent (see also Ciardi & Madau 2003). For example, in the Ly α heating case, at an early stage (dashed lines), when most of the signal comes from completely neutral regions, only one peak is visible in absorption, corresponding to $\delta T_{b,\text{peak}} \approx -150$ mK. However, as ionization proceeds, the amplitude of the peak decreases and moves toward a positive value; meanwhile, a new, smaller peak appears with positive value at $\delta T_b \sim$ several mK, which comes from the partially ionized regions (see the dashed and dashed-dotted lines in Fig. 11 and Fig. 12). The three redshifts chosen show three typical situations: when the totally neutral regions dominate, when the partially ionized regions begin to produce a significant signal and when the contribution from partially ionized regions is more evident, respectively. The behavior of

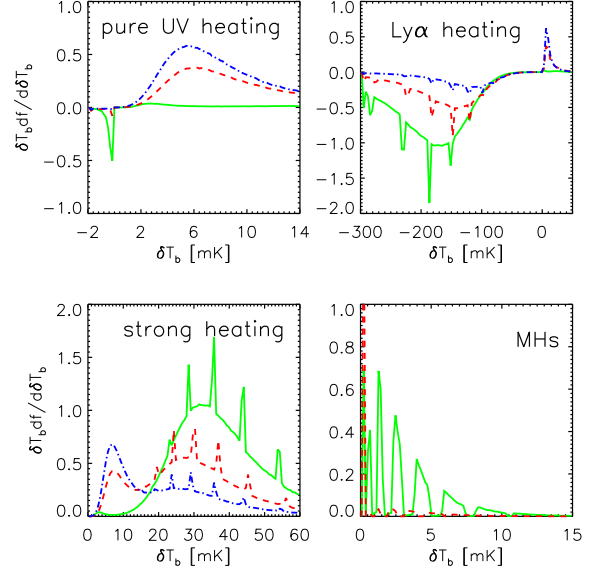


Figure 11. Pixel distribution for both the IGM and minihalos for the extreme suppression model. Different lines correspond to different redshifts. In each IGM panel, solid, dashed and dashed-dotted lines mean redshift 18.1, 15.5, 14.8 respectively. In the minihalos panel instead, pixel distribution is given at redshift 16.6 (solid) and 13.7 (dashed).

the pixel distribution is very similar for the extreme suppression and the reformation model, the only difference being a delay in the reformation model. In the $T_s \gg T_{\text{CMB}}$ case, the trend is the same as in the Ly α heating case, i.e. as ionization proceeds, the peak corresponding to the totally neutral regions decreases and moves toward zero, while the peak originating from the partially ionized regions increases. However, the situation is slightly different in the pure UV heating case, in which the contributions from the partially ionized regions become significant at an earlier stage.

Finally, the dominant minihalo contribution at all redshifts comes from cells with $\delta T_b \approx 1\text{--}2$ mK, which is a typical value of beam-averaged differential brightness temperature in our simulation (this value depends on the cosmological parameters and the matter power spectrum, see Iliev et al. 2002). Unlike the IGM signal, here there is always only one peak; however, since we can measure only a total flux, this feature is not useful to distinguish the signal of minihalos from that of the IGM. The sawtooth features come from the discreteness effect introduced when calculating f_{MH} , which shows also in the spikes of the IGM signal.

3.3 Model uncertainties

In this Section we discuss the main approximations and uncertainties of our model and their impact on the results, in addition to those already discussed in C06.

- In the pure UV heating case, partially ionized regions contribute significantly to the emission signal. However, we note that the resolution of our simulation is only ≈ 223 kpc, which is not enough to resolve the I-front. This leads to the possibility of overestimating the signal from partially ionized regions by mixing together totally ionized and totally

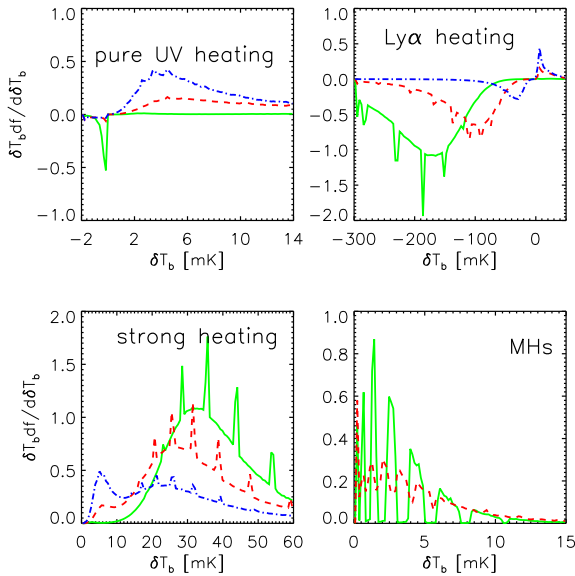


Figure 12. Same as Fig. 11, but for the reformation model. In each IGM panel, solid, dashed and dashed-dotted lines mean redshift 18.1, 14.2 and 12.2 respectively, while in the minihalos panel, solid line refers to redshift 16.6 and dashed line refers to redshift 11.1.

neutral regions. In fact there are many uncertainties related to the sub-grid neutral filling factor, including the inhomogeneity of the density field on small scales and the spectrum of the sources (e.g. Iliev et al. 2006).

In our work we refer to “partially ionized” cells as regions heated by UV photons that still contain enough neutral hydrogen to emit a 21 cm signal. Note that this somewhat arbitrary definition is used only to estimate the relative contribution of gas in different physical conditions, while all the cells in the simulation have been used to calculate the total 21 cm signal. In all our previous calculations, we identified partially ionized cells as those with ionization fraction x above a threshold value of 0.1, but a value of 0.01 leads to similar results. If x is very close to 1.0, the signal from a cell is negligible and the cell is referred to as totally ionized.

If we assume that in a partially ionized cell only a fraction f_{pi} of the gas is partially ionized with an ionization fraction of x_{pi} , while the rest is either neutral and cold, or ionized and hot and thus irrelevant for the contribution from the partially ionized regions. Furthermore, we should consider that only a fraction of gas $f_{pi} \times (1 - x_{pi})$ is contributing to the signal. Both f_{pi} and x_{pi} are unknown, and vary in a large range cell by cell. As a reference, if we assume $x_{pi} = x$ we find that at the redshift when half of the gas has been ionized, the mean δT_b of the total simulation volume for f_{pi} equal to (0.0, 0.001, 0.01, 0.05, 1.0) are (-0.054, -0.051, -0.012, 0.21, 5.63) mK respectively for the extreme suppression case. Note that $(f_{pi}, \delta T_b) = (1.0, 5.63 \text{ mK})$ corresponds to the peak of the dashed line in upper panel of Fig. 6.

So if the sub-grid neutral filling factor is much lower than 1.0, we expect no emission mean signal or non-dominant partially ionized IGM signal in the pure UV heating case. However, the pure UV heating model ignores the pre-heating by X-rays and Ly α photons, thus we expect it to be appro-

priate to describe only the early stages of reionization. Also the small emission in the Ly α coupling case suffers from this uncertainty, although our main trends and conclusions will not change. Finally, in the strong heating case, the influence of resolution should be negligible. This is natural since in those two models, the dominant signal is from the neutral gas.

- To derive the mass evolution of MHs undergoing photoevaporation we use the fitting formula by Iliev et al. (2005). The formula reproduces the results from their numerical simulation, but it is approximate. Moreover, it is accurate only for a constant ionization flux, while in the simulations by C06, the flux assumes different values at different times and locations. We tried two different methods to derive eq. (11) in the presence of a time dependent flux, corresponding to eq. (12) and eq. (14), which consistently predict the δT_b within few percent. As in C06, for most halos, the evaporation time is comparable or smaller than the time between two outputs (for example, in the extreme suppression model $\approx 66\%$ of the cells lose 80% of their MH mass between two outputs). We also do not expect the use of those formulae to introduce uncertainties in addition to those already present in the C06 implementation.

- To calculate the 21 cm flux from an individual minihalo we use the formula from Iliev et al. (2002) and then we integrate over the mass function in eq. (10) to obtain the beam-averaged effective differential brightness temperature of eq. (8). This formula is only suitable for halos that are in post-collapse equilibrium with a TIS profile. Yet, when a halo is being photoevaporated, both its density and temperature profile may be substantially different³. The new profile should depend on the local ionization flux. If we define the dynamical timescale as $t_{\text{dyn}} = \pi r_{\text{TIS}}/v_c$, where v_c is the halo circular velocity, for a halo with mass $10^7 M_\odot$ at redshift 15, $t_{\text{dyn}} \approx 150 \text{ Myr}$ while $t_{\text{ev}} \approx 230 \text{ Myr}$ if $F_0 = 1$. So the timescales are comparable and the halo profile could be changed during photoevaporation. In fact, also Iliev et al. (2005) notice that the typical evaporation time is long enough to see a gas-dynamic back-reaction. Since the effects of this change on the 21 cm signal of MHs is still not clear, we ignore the effect in this work. In addition, heating of the IGM can also change the profile of a halo, make it less concentrated and thus increase the 21 cm signal (Oh & Haiman 2003). On the other hand, the equation $T_s \gg T_{\text{CMB}}$ will always be satisfied, so the impact of the temperature change on the 21 cm signal should be much less than that of the change on the density profile.

4 CONCLUSIONS

We have studied the 21 cm signal from both the IGM and minihalos based on the reionization simulations run by Ciardi et al. (2006). These include a “sub-grid” prescription to take into account the photoevaporation of MHs in two different models for their formation (extreme suppression and reformation). Our estimates follow the changes in the mass function of MHs and consider three heating case of the IGM. We find that:

³ And in general, also if undisturbed, the halo could follow a different shape (e.g. Navarro, Frenk & White 1997).

- the 21 cm signal tightly relates to the thermal history of the IGM. In all the three configurations (heating purely by the UV photons, Ly α and UV heating, and strong heating), the IGM dominates the 21 cm signal at almost all redshifts, except at a very early stage when the gas is still cold and a Ly α background has not been constructed or at the end of reionization in the reformation model, when almost all the remaining neutral gas is in MHs. The small contribution of minihalos to the total 21 cm flux is partially due to the fact that the collapsed fraction of MHs is relatively small at high redshift. Minihalos are significant emission sources in the absence of IGM heating, however, in partially ionized regions which are heated by UV photons, where there is enough residual neutral gas and the temperature is much larger than T_{CMB} , the IGM also provides a contribution to the emission signal. In the presence of a Ly α background, neutral gas will be visible in strong absorption until a later stage when neutral regions are rare. In such case, totally neutral regions contribute more than partially ionized regions and MHs to the total 21 cm signal.

- Although MHs are directly visible in 21 cm signal only under particular circumstances, they nevertheless play a significant role in affecting the ionization state of the IGM and the corresponding 21 cm flux. Their presence can delay reionization by as much as $\Delta z \approx 4$, depending on the effect of feedback on their formation (C06). More specifically, in the pure UV heating case, the 21 cm signal from the IGM in the reformation model is weaker than that in extreme suppression model at the same redshift, since MHs delay the photoheating associated with reionization. In the strong heating case on the other hand, the 21 cm emission is higher in the reformation model than in the extreme suppression model at the same redshift, because absorption from MHs leaves more neutral gas in the IGM. This difference shows that in the pure UV heating case, the temperature is the most important factor which can impact the δT_b of the IGM, while in the strong heating case the most important factor is n_{HI} .

- While the 21 cm signal from MHs exhibits differences from the IGM signal, including the pixel distribution, detecting such features will not be within the capabilities of the planned generation of radio telescopes (e.g. LOFAR⁴, MWA⁵, 21cmA⁶). In principle, MHs are more abundant in rich cluster regions, which implies a higher 21 cm signal. In practice, in these regions also contain more ionizing sources that suppress MHs formation and evolution, reducing their signal.

Conclusions similar to those derived from our simulations have been reached by previous analytic estimates (e.g. Oh & Mack 2003; Furlanetto & Oh 2006). For example, Furlanetto & Oh (2006) calculated the signal from both the IGM and the minihalos, using a semi-analytic approach that includes the X-ray heating and feedback effects on halo formation. They found that in the presence of Wouthuysen-Field coupling, MHs are always buried by the IGM signal, even if the Ly α background is small. On the other hand, Shapiro et al. (2006) concluded that before reionization but

after $z \approx 20$, ignoring the radiative processes but taking into account shock heating, minihalos could dominate the total signal. This conclusion is consistent with our pure UV heating case at the early stage.

5 ACKNOWLEDGMENTS

We thank Ilian T. Iliev, Jordi Miralda-Escude, and Yidong Xu for helpful discussions. ES thanks the Max Planck Institute for Astrophysics for their hospitality. XC is supported by the NSFC Distinguished Young Scholar Grant No.10525314, Key Grant No. 10503010, by the CAS grant No. KJCX3-SYW-N2, and by the MoST 973 project grant No.2007CB815491.

REFERENCES

- Ahn K., Shapiro P. R., 2007, MNRAS 375, 881
 Ali S. S., Bharadwaj S., Panday B., 2005, MNRAS, 363, 251
 Barkana R., Loeb A., 2002, ApJ, 578, 1
 Chen X., Miralda-Escudé J., 2004, ApJ, 602, 1
 Chen X., Miralda-Escudé J., 2008, ApJ, 684, 18
 Chuzhoy L., Shapiro P. R., 2006, ApJ, 651, 1
 Chuzhoy L., & Shapiro P. R., 2007, ApJ, 655, 843
 Ciardi B., Ferrara A., Governato F., Jenkins A., 2000, MNRAS, 314, 611
 Ciardi B., Ferrara A., Marri, S., Raimondo G., 2001, MNRAS, 324, 381
 Ciardi B., & Madau, P., 2003, ApJ, 596, 1
 Ciardi B., Stoehr, F., White, S. D. M., 2003, MNRAS, 343, 1101
 Ciardi B., Ferrara A., White S. D. M., 2003, MNRAS, 344, 7
 Ciardi B., Ferrara A., 2005, Space Science Reviews, 116, 625
 Ciardi B., Scannapieco E., Stoehr F., Ferrara A., Iliev I. T., Shapiro P. R., 2006, MNRAS, 366, 689 (C06)
 Ciardi B., & Salvaterra, R., 2007, MNRAS, 381, 1137
 Cooray A., Li C., Melchiorri A., 2008, astro-ph/0801.3463
 Efstathiou, G., Bond, J. R., White, S. D. M., 1992, MNRAS, 258, 1
 Field, G. B., 1958, Proc. IRE, 46, 240
 Furlanetto S. R., Loeb A., 2002, ApJ, 579, 1
 Furlanetto S. R., Sokasian A., Hernquist L., 2004, MNRAS, 347, 187
 Furlanetto S. R., Zaldarriaga M., Hernquist L., 2004, ApJ, 613, 16
 Furlanetto S. R., Loeb A., 2004, ApJ, 611, 642
 Furlanetto S. R., & Oh S. P., 2006, ApJ, 652, 849
 Furlanetto S. R., Oh, S. P., Briggs F. H., 2006, PhR, 433, 181
 Furlanetto S. R., Pritchard J. R., 2006, MNRAS, 372, 1093
 Gnedin N. Y., 2000, ApJ, 542, 535
 Haiman Z., Rees M. J., Loeb A., 1997, ApJ, 476, 458 (erratum 484 985)
 Haiman Z., Abel T., Rees M. J., 2000, ApJ, 534, 11
 Haiman Z., Abel T., Madau P., 2001, ApJ, 551, 599
 He P., Liu J., Feng L-L., Bi H-G., Fang L-Z., 2004, ApJ, 614, 6

⁴ <http://www.lofar.org/>

⁵ <http://www.haystack.mit.edu/mwa/index.html>

⁶ <http://21cma.bao.ac.cn/>

- Hockney R. W., Eastwood J. W., 1981, in "Computer Simulations Using Particles"; New York: McGraw-Hill
- Iliev I. T., Shapiro P. R., 2001, MNRAS, 325, 468
- Iliev I. T., Shapiro P. R., Ferrara A., Martel H., 2002, ApJ, 527L, 123
- Iliev I. T., Shapiro P. R., Raga, A. C., 2005, MNRAS, 361, 405
- Iliev I. T., et al., 2006, MNRAS, 371, 1057
- Kauffmann G., Colberg J. M., Diaferio A., White S. D. M., 1999, MNRAS, 303, 188
- Kramer R. H., Haiman Z., Oh S. P., 2006, ApJ, 649, 570
- Kuhlen M., Madau P., Montgomery R., 2006, ApJ, 637L, 1
- Lacey C., Cole S., 1993, MNRAS, 262, 627
- Lewis A., Challinor A., 2007, Phys Rev D, 76, 083005
- Loeb A., Zaldarriaga M., 2004, Phys. Rev. Lett., 92, 1301
- Madau P., Meiksin A., Rees M. J., 1997, ApJ, 475, 429
- Mao Y., et al., 2008, astro-ph/0802.1710
- Maselli A., Ferrara A., Ciardi B., 2003, MNRAS, 345, 379
- Maselli A., Ciardi B., Kanekar A., 2008, MNRAS, in press
- Meiksin A., 2006, MNRAS 370, 2025.
- Mellema G., Iliev I. T., Pen U., Shapiro P. R., 2006, MNRAS, 372, 679
- Miniati F., Ferrara A., White S. D. M., Bianchi S., 2004, MNRAS, 348, 964
- Mo H. J., White S. D. M., 1996, MNRAS, 282, 347
- Navarro J. F., Frenk C. S., White S. D. M., 1997, ApJ, 490, 493
- Nusser A., 2005, MNRAS, 359, 183
- Oh S. P., 2001, ApJ, 553, 499
- Oh S. P., Haiman Z., 2003, MNRAS, 346, 456
- Oh S. P., & Mack K. J., 2003, MNRAS, 346, 871
- Pillepich A., Porciani C., Matarrese S., 2007, ApJ, 662, 1
- Pritchard J. R., Furlanetto S. R., 2007, MNRAS, 376, 1680
- Ripamonti E., Mapelli M., Zaroubi S., 2008, astro-ph/0802.1857
- Rybicki, G. B., 2006, ApJ, 647, 709.
- Santos M. G., Cooray A., Knox L., 2005, ApJ, 625, 575
- Santos M. G., Amblard A., Pritchard J., Trac H., Cen R., Cooray A., astro-ph/0708.2424
- Seager S., Sasselov D. D., Scott D., 1999, ApJ, 523, L1
- Seager S., Sasselov D. D., Scott D., 2000, ApJS, 128, 407
- Semelin B., Combes F., Baek S., 2007, A&A, 474, 365
- Shapiro P. R., Giroux M. L., Babul A., 1994, ApJ, 427, 25
- Shapiro P. R., Raga A. C., Mellema G., 1997, seim.proc, 41
- Shapiro P. R., Iliev I. T., Raga A. C., 1999, MNRAS, 307, 203
- Shapiro P. R., Raga A. C., 2000, RMxAC, 9, 292
- Shapiro P. R., Iliev I. T., Raga A. C., 2004, MNRAS, 348, 753
- Shapiro P. R., Ahn K., Alvarez M. A., Iliev I. T., Martel H., Ryu D., 2006, ApJ, 646, 681
- Sheth R. K., Tormen G., 2002, MNRAS, 329, 61
- Tozzi P., Madau P., Meiksin A., Rees M. J., 2000, ApJ, 528, 597
- Whalen, D., Prochaska, J. X., Heger, A., & Tumlinson, J. 2008, ApJ, in press (arXiv:0802.0737)
- Wouthuysen S. A., 1952, AJ, 57, 31
- Yoshida N., Sheth R. K., Diaferio A., 2001, MNRAS, 328, 669
- Zaldarriaga M., Furlanetto S. R., Hernquist L., 2004, ApJ, 608, 622